Article:
van den Heever, SP, van der Walt, DJ, Pittard, JM orcid.org/0000-0003-2244-5070 et al. (1 more author) (2019) Periodic methanol masers: from a colliding wind binary (CWB) perspective. Monthly Notices of the Royal Astronomical Society, 485 (2). pp. 2759-2771. ISSN 0035-8711

https://doi.org/10.1093/mnras/stz576

Monthly Notices
of the
ROYAL ASTRONOMICAL SOCIETY

MNRAS **485,** 2759–2771 (2019)
Advance Access publication 2019 March 6

doi:10.1093/mnras/stz576

Periodic methanol masers: from a colliding wind binary (CWB) perspective

S. P. van den Heever,[1]★ D. J. van der Walt,[1]★ J. M. Pittard[2] and M. G. Hoare[2]

[1]*Center for Space Research, North West University, Potchefstroom 2520, South Africa*
[2]*School for Physics and Astronomy, Univeristy of Leeds, LS2 9JT, UK*

Accepted 2019 February 25. Received 2019 February 25; in original form 2018 November 28

ABSTRACT

Since the discovery of periodic class II methanol masers at 6.7 and 12.2 GHz associated with high-mass star formation regions (HMSFRs), a number of possible driving mechanisms have been proposed to explain this phenomenon. Here, we apply a more realistic treatment of the original colliding wind binary (CWB) model explanation to investigate to what extent it can describe the flare profiles of the periodic methanol masers. It was found that the CWB hypothesis is feasible from an energetics standpoint, because the emission from the shocked gas does cause an outward shift of the position of the ionization front (IF). This confirms that the energy budget available from the shocked gas is enough to be the driving force behind the CWB model. The CWB model describes the light curve of the 1.25 km s^{-1} 12.2 GHz velocity feature of G9.62 + 0.20E very well over 4000 d. The quiescent state flux density of the 1.25 km s^{-1} velocity feature can also be described very well by the time-dependent change in electron density (n_e). The CWB model also describes the other periodic methanol masers, G22.357 + 0.066, G37.55 + 0.20, and G45.473 + 0.134, which have similar light curves, very well. This strongly suggests that these periodic methanol masers can be described by the time-dependent change in the free–free emission from some part of the background H II region against which the masers are projected.

Key words: hydrodynamics – masers – H II regions – ISM: molecules – radio lines: ISM – X-rays: binaries.

1 INTRODUCTION

Since the discovery of the bright and widespread class II methanol masers at 12.2 (Batrla et al. 1987) and 6.7 GHz (Menten 1991), there has been an increased interest in the field of astronomical masers. It is now rather firmly established that the class II methanol masers are exclusively associated with high-mass star formation regions (HMSFRs, see e.g. Ellingsen 2006; Breen et al. 2010, 2013). In spite of their association with HMSFRs and H II regions, there is still no clear picture of where in the circumstellar environment these class II methanol masers arise (see e.g. van der Walt, Sobolev & Butner 2007). Observations done by e.g. Norris et al. (1993) and Bartkiewicz et al. (2009) suggest that they might be located in a circumstellar disc or torus. On the other hand, some authors are of the opinion that these masers are associated with outflows (e.g. Minier et al. 2000; De Buizer 2003). Regardless of where in the circumstellar environment the masers reside, single-dish monitoring of class II masers has proved to be rewarding. From the monitoring of 54 class II methanol masers with the 26-m Hartebeeshoek Radio telescope, seven were found to show periodic/regular variability (see Goedhart, Gaylard & van der Walt 2003, 2004, 2007; Goedhart et al. 2009). Since this initial discovery, a number of additional periodic sources have been discovered (see e.g. Araya et al. 2010; Fujisawa et al. 2014; Szymczak et al. 2011; Szymczak, Wolak & Bartkiewicz 2015; Maswanganye et al. 2015, 2016). Simultaneous quasi-periodic flaring of methanol and formaldehyde masers have also been recorded in IRAS 18566 + 0408 (Araya et al. 2010). Except for the simultaneous periodic flares of hydroxyl associated with G9.62 + 0.20E (Goedhart, private communication) and the case of IRAS 18566 + 0408, no other masing species associated with HMSFRs have yet been found that show periodic variability.

Whether the periodic variability arises from changes in the masing region itself or the background radiation field still remains an unresolved issue. Very Long Baseline Array observations of G9.62 + 0.20E show no structural changes of the masers between the quiescent phase and during a flare event. The maser flux density also returns to almost the same pre-flare level after each flare, which strongly suggests that a cause external to the masing region is responsible for the flares (Goedhart et al. 2005). Goedhart et al. (2005) therefore argue that the flares are not caused by a physical disturbance, such as a shock wave, which would cause changes

★ E-mail: fanie@hartrao.ac.za (SPH); johan.vanderwalt@nwu.ac.za (DJW)

to the masing region. This leaves two general possibilities for the origin of the flare: either an increase in the seed photon flux or a change in the pumping radiation field.

Within this context, several hypotheses have been proposed to explain the periodic variability of the methanol masers in G9.62 + 0.20E. Araya et al. (2010) ascribe the periodic variability of the formaldehyde and methanol masers in IRAS 18566 + 0408 (G37.55 + 0.20) to periodic accretion events of circumbinary disc material in a very young binary system that heats the dust and therefore changes the pumping radiation field. These authors argue that such a scenario might also be applicable to G9.62 + 0.20E. Numerical calculations by van der Walt (2014) suggest that these two species are pumped by different mechanisms and that it is therefore unlikely that the observed correlated variability is due to the periodic changes in the pumping radiation field. Parfenov & Sobolev (2014) also suggest the presence of a binary system, however, in their model, it is the emission from rotating spiral shocks in the gap of a circumbinary disc that heats the dust periodically. Inayoshi et al. (2013) suggested that pulsations of the young high-mass star might lead to time-dependent changes in the dust temperature and therefore also changes in the pumping radiation field. Following the results of Inayoshi et al. (2013), Sanna et al. (2015) suggested that the periodic variability of the class II methanol masers associated with G9.62 + 0.20E might be due to a pulsating young massive star. van der Walt et al. (2016) investigated to what extent these models can explain the periodicity of these masers, and found that none of these models could reproduce the observed maser flares in G9.62 + 0.20E.

Considering the decay part of the 12.2 GHz methanol maser flares in G9.62 + 0.20E, van der Walt, Goedhart & Gaylard (2009) and van der Walt (2011) suggested that the flares might be due to changes in the background free–free emission from the H II region. These authors showed that the decay of the 12.2 GHz masers can be described very well by what would be expected of the free–free emission from a recombining hydrogen plasma. To explain the increase in the level of ionization, van der Walt et al. (2009) and van der Walt (2011) postulate the presence of a very young colliding wind binary (CWB) system. In this scenario, the orbital motion of the binary system modulates the production of copious amounts of ionizing photons produced by the hot ($\geq 10^6$ K) shocked gas of the CWB system, resulting in a 'pulse' of ionizing photons. The pulse of ionizing photons propagates virtually unattenuated through the ionized gas to the ionization front (IF), where it results in a small outward shift in the position of the IF. The outward shift of the IF is a result of the increase of the electron density in the partially ionized gas, against which the maser is proposed to be projected. The maser 'sees' an increase in the free–free emission followed by a characteristic decay due to the recombination of the plasma to its equilibrium state as determined by the ionizing flux from the young high-mass star.

To investigate the basic aspects of the CWB scenario, van der Walt (2011) used a toy model, which takes into account some general aspects of such a CWB system, and applied it to the 1.25 km s^{-1} velocity feature of the 12.2 GHz methanol maser in G9.62 + 0.20E. Although the toy model was found to describe the flare profile rather well, it lacked in at least two ways. First, to enable easy calculation, it was assumed that the shocked gas cools adiabatically through the entire orbit, i.e. the radiative luminosity of the shocked gas behaved like $L_{\rm shock} \propto D^{-1}$ (Stevens, Blondin & Pollock 1992), with D the separation between the stars. The possibility of the gas cooling radiatively has therefore not been taken into account. Second, the effect of the pulse of ionizing radiation was modelled as a change in the ionization rate at the IF, without a physical justification that the change in ionization rate is energetically possible. To justify the CWB scenario from a theoretical point a more realistic calculation of the behaviour of the shocked gas is required. This will also allow for the calculation of the spectral energy distribution (SED) of the radiation emitted by the shocked gas and its effect on the IF.

In this work, the shocked gas is simulated hydrodynamically and whether the shocked gas cools adiabatically or radiatively is determined self-consistently in the simulations. The physical conditions of the shocked gas are used to calculate the emergent total emission and SED. In this way, the SED produced from the shocked gas depends both on the separation distance and whether it cools adiabatically or radiatively. The SED together with the radiation field of the primary star are used to do the radiative transfer calculations using the photoionization code CLOUDY (Ferland et al. 1998). For the projection of the maser spot on the IF, the time-dependence of the electron density ($n_{\rm e}(t)$) is solved for, with the results from the CLOUDY simulations. In the optically thin limit, i.e. $I_\nu \propto n_{\rm e}^2$, this describes the time-dependent change in the free–free emission proposed to explain the periodic changes of the methanol masers. It is shown that the CWB model reproduces the 1.25 km s^{-1} velocity feature of the 12.2 GHz methanol maser time-series of G9.62 + 0.20E very well over a span of 4000 d. It also reproduces the 6.7 GHz methanol maser time-series of G22.357 + 0.066, and describes the average flare profiles of G37.55 + 0.20 and G45.473 + 0.134 very well. In addition, the time-dependent change in the quiescent state flux density of the 1.25 km s^{-1} velocity feature of the 12.2 GHz methanol maser in G9.62 + 0.20E can be described very well by the time-dependent change of the quiescent state electron density obtained. The numerical components of the CWB model will be discussed in Section 2, and Section 3 will discuss the approach followed to derive the electron densities associated with the flares. In Section 4, the results will be shown, in Section 5, the results will be discussed, and in Section 6, conclusions will be drawn.

2 NUMERICAL APPROACH

The basic framework of the CWB model has been given in van der Walt (2011). Here, a more realistic approach will be followed, and the individual components that make up the 'full' model will be described.

2.1 CWB model parameters

From the methanol multibeam surveys (Caswell et al. 2010, 2011; Green et al. 2010, 2012) $\simeq$1000 class II methanol masers have been found associated with HMSFRs. Assuming that the multiplicity of massive stars in HMSFRs resemble that which have been found visually and spectroscopically (see the survey of e.g. Mason et al. 1998), it is reasonable to assume that there is a population of HMSFRs (with associated methanol masers), which harbour binary systems. Thus, we used *Kepler*'s three laws to calculate a binary orbit in the reference frame of the primary star, where the primary is located at one of the focii of the ellipse. To calculate the orbit, we need information on the mass, period, and eccentricity of the binary system. Unfortunately, we have no observational evidence of any of these parameters. The exception, in this case, is that the periodicity explicitly implies the period of the binary system. For the total mass of the binary system, we can obtain reasonable parameters from theoretical models and observations. The eccentricity will follow from *Kepler*'s laws.

Table 1. The table first shows the three models CWB1, CWB2, and CWB3 with the combinations of stellar parameters used to simulate the colliding winds for each. Here, $\dot{M}_1$ and v_1 are the mass-loss rate and stellar wind velocity for the primary star, and $\dot{M}_2$ and v_2 for the secondary, respectively. The mass-loss rates are defined in units of $M_\odot$ yr^{-1}, and the stellar wind velocities are defined in units of cm s^{-1}. Additionally, it shows the range of stellar types considered with their surface temperatures, $T_{\rm eff}$ in kelvins, and the ionizing photon rate $Q(H)$. It also shows the molecular cloud densities from 4 to 7 $\times$ 10^6 cm^{-3} (with an interval of 10^6 cm^{-3}) used to simulate the H II region.

Variables (units)	CWB 1	CWB 2	CWB 3
$\dot{M}_1$ ($M_\odot$ yr^{-1})	1×10^{-6}	9×10^{-7}	8×10^{-7}
$\dot{M}_2$ ($M_\odot$ yr^{-1})	8×10^{-7}	6×10^{-7}	6×10^{-7}
$v_{1,\infty}$ (cm s^{-1})	1.6×10^8	1.6×10^8	1.6×10^8
$v_{2,\infty}$ (cm s^{-1})	1.2×10^8	1.2×10^8	1.2×10^8
Stellar type	$T_{\rm eff}$ (K)	ρ ($\times$ 10^6 cm^{-3})	lg($Q(H)$ s^{-1})
B0	33 340	4–7	48.02
O9.5	34 900	4–7	48.29
O9	35 900	4–7	48.47
O8.5	36 840	4–7	48.61
O8	37 170	4–7	48.75

To simulate the colliding winds, the mass-loss rates and the stellar wind speeds of the two stars are needed. Fortunately G9.62 + 0.20E has been studied extensively in the past, and various observations are available. The observations of Hofner et al. (1996) and Testi et al. (2000) were used. From their analysis of the continuum between 2.7 mm and 3.6 cm and the methylcyanide (CH_3CN) line emission, the estimated spectral type of the early-type star is approximately an O9.5 star. Correcting for the contribution from dust emission with a temperature of $\simeq$100 K (Hofner et al. 1996), they adopted a star with stellar type B1–B0. Similarly, for the other HMSFRs, the spectral type of the primary star is estimated where observations are available. Within the CWB scenario and the mass–luminosity relation, $L \approx M^{3.5}$ (see e.g. Kuiper 1938), there are two possibilities, (1) two stars with equal mass which are equivalent in luminosity to a B0 star, or (2) the primary, a B0 star, where the companion has a mass which makes a negligible contribution to the total luminosity. Using the estimated spectral type, the mass-loss rate (Sternberg, Hoffmann & Pauldrach 2003; Vink, de Koter & Lamers 2000), stellar wind speed (Bernabeu, Magazzu & Stalio 1989; Sternberg et al. 2003), mass (Panagia 1973; Sternberg et al. 2003), and surface temperature (Panagia 1973; Sternberg et al. 2003) could be inferred. Additionally, in order to investigate a larger portion of parameter space and account for different spectral types (for the cases where no information could be found), stars with spectral type B0–O8 were considered. The observations of Bernabeu et al. (1989) were used to estimate the stellar wind speeds for the entire set of stars considered. These observations show that the stellar wind speeds of stars B0–O8 overlap to a large extent, with values of 1600 $\pm$ 610 km s^{-1}.

Considering the above information, three models CWB1, CWB2, and CWB3, with the combinations of their stellar parameters, are summarized in Table 1. For (1) with two identical stars of spectral type B0.5, which is approximately equivalent to a B0 star (Sternberg et al. 2003), the total mass of the system is assumed as $\simeq$ 38 $M_\odot$. Including the effect of other spectral types and (2) above, we consider total system masses from 30 to 40 $M_\odot$. Note that the orbit depends weakly on the total mass, it should not affect the orbit too much. Table 1 also gives the stellar and molecular cloud parameters used to simulate the H II region (which the primary star maintains).

2.2 Hydrodynamical simulations

The shocked gas of the CWB system was simulated using the hydrodynamic code ARWEN (developed by Julian Pittard), based on the VH-1 code (Blondin & Stevens 1990, and coworkers). The code was set-up to simulate the colliding stellar winds as done in the work of Stevens et al. (1992). It uses a 2D cylindrically symmetric grid with the stars represented as two stationary points a distance D apart. The stellar winds are set to be spherically symmetric, and to emanate from these two stationary points equidistant on either side of the mid-plane of the grid. The winds are initiated at these two locations, with their fixed terminal velocities and density mapped on to a few cells around the centre of each star. This is called the remap radius. The remap radius puts a constraint on the minimum separation distance between the two stars that can be simulated; the separation must be greater than twice the remap radius. The simulations were carried out for all combinations of mass-loss rate and stellar wind speed given in Table 1. In order to construct a binary orbit, the calculations were done for 40 separation distances between 0.5 and 4.5 au (with intervals of 0.1 au).

The calculation of the shocked gas was carried out for a simulation time of 10^7 s. For shocked gas cooling adiabatically, it takes $\approx$3 $\times$ 10^6 s to reach an equilibrium state. The extended calculation time is invoked when radiative cooling dominates, and no equilibrium state is reached. This extended calculation time enables the calculation of a statistical average from several 'snapshots' when the shocked gas is dominated by radiative cooling. To be consistent, the statistical average is used for both adiabatic and radiative cooling. The conditions that control whether or not the shocked gas cools radiatively or adiabatically are discussed in detail in Stevens et al. (1992). Fig. 1 shows example 'snapshots' for both adiabatically cooling (top panel) and radiatively cooling (bottom panel) shocked gas.

2.3 Plasma emission

The intrinsic emission from the shocked gas is obtained by summing the emission from each cell. This is calculated from the volume and emissivity of each cell. The volume of each cell is that of an annulus around the symmetry axis, given the coordinates and dimensions of the cell. In order to calculate the emission produced from each cell, the temperature is obtained using the ideal gas law:

$$T = \frac{P\mu}{\rho k}, \quad (1)$$

where μ is the mean molecular weight of the gas, k is Boltzmann's constant, P is the pressure, and ρ is the density.

Given the temperature, the relevant volumetric emissivity is obtained from a look-up table calculated using the MEKAL plasma code (see e.g. Kaastra & Mewe 2000, and references therein). The look-up table consists of 300 logarithmically spaced energy bins in the range 0.01–10 keV, and 101 logarithmically spaced temperature bins for the range 10^4–10^9 K. The emission is calculated with the volume and the density for all cells with temperatures above the hydrogen ionization threshold temperature of $\simeq$1.5 $\times$ 10^5 K ($\simeq$13.6 eV). Summing the emission over all the cells that satisfy this criterion gives the total intrinsic luminosity emitted from the shocked gas (i.e. the shocked gas and the stellar winds are assumed to be optically thin and absorption is assumed to be negligible). The

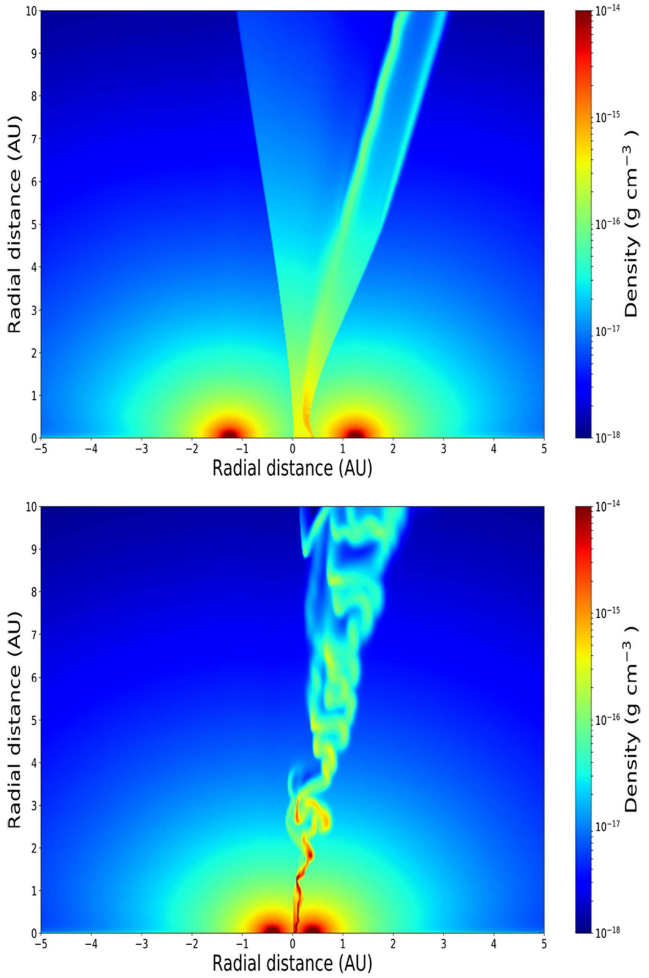

Figure 1. Two examples of the hydrodynamical simulations of the shocked gas. Top panel: a 'snapshot' representing gas cooling adiabatically with a smooth flow away from the shock apex, with a separation distance of 2.5 au. Bottom panel: a 'snapshot' of gas dominated by radiative cooling for a separation distance of 0.7 au. The colour scale is the logarithm of the density in g cm^{-3}.

SEDs and luminosities were calculated for all three models given in Table 1.

2.4 Photoionization calculations

The photoionization code CLOUDY was used to perform the calculations to determine whether the ionizing photons generated from the shocked gas can cause significant enough additional ionization at the IF. The H II region is firstly simulated by assuming that the primary star radiates as a blackbody (BB), ie. the radiation field which maintains the H II region. The BB spectrum of the star is defined by the surface temperature ($T_{\rm eff}$) and the production rate of the ionizing photons $Q(H)$, taken from the theoretical model of Sternberg et al. (2003) as given in Table 1. The SED produced by the hot shocked gas is added to the stellar spectrum to determine its possible influence at the IF. These simulations were performed for several constant neutral hydrogen densities, several spectral types of the primary star, the three mass-loss rate combinations, and for each of the 40 stellar separations. Fig. 2 shows examples of both a BB (black line) spectrum and a combined (BB and shocked gas SED, blue line) spectrum.

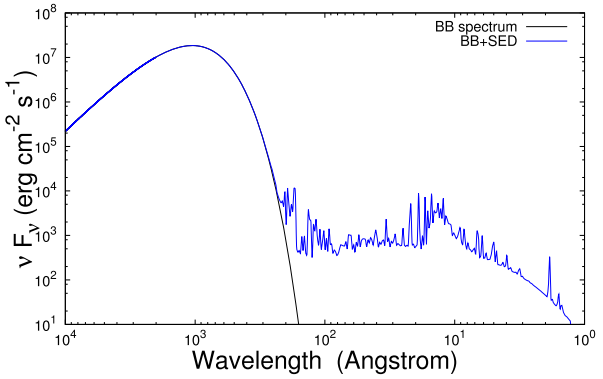

Figure 2. Example of the SED of a BB with effective surface temperature of $T_{\rm eff}$ = 33340 K (black line), and the combined SED of the BB and an additional spectrum from the shocked gas of the colliding stellar winds (blue line).

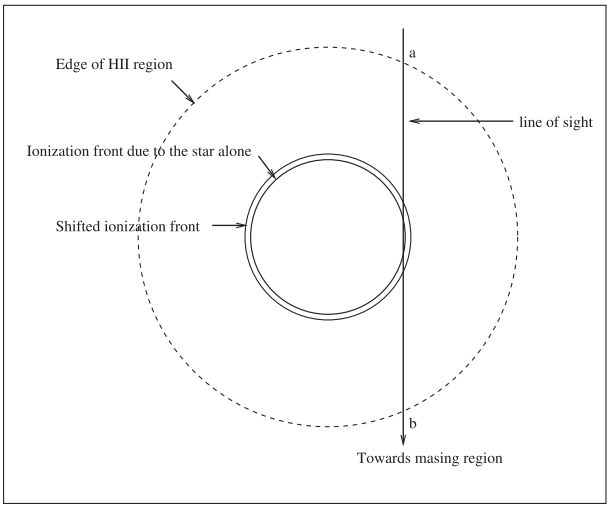

Figure 3. A schematic representation of the line of sight through the H II region at the tangent point of the sphere representing the IF. The inner solid sphere representing the IF due to the star alone, the outer solid sphere represents the IF shifted by the additional IF, and the outer dashed sphere representing the outer edge of the H II region. Remember that this is not to scale.

2.5 Time-dependent free–free emission from the IF

The equilibrium solutions obtained for the positions of the IF from the CLOUDY simulations were used to construct a quasi time-dependent solution of the position of the IF (orbital separation between the stars). The periodic variation of the position of the IF is caused by the additional periodic change in the flux of ionizing photons from the shocked gas of the colliding winds. The maser is proposed to be projected against the IF, which is illustrated in Fig. 3, where the line of sight of the maser spot is along the line from a to b. In the optically thin case, the time-dependent free–free emission then follows from the time dependence of the electron density in the partially ionized gas of the IF, using:

$$\frac{{\rm d}n_{\rm e}}{{\rm d}t} = -n_{\rm e}^2\beta + \Gamma(t)n_{\rm H_0}, \quad (2)$$

(see van der Walt et al. 2009; van der Walt 2011) where β is the recombination coefficient, Γ(t) the time-dependent ionization rate,

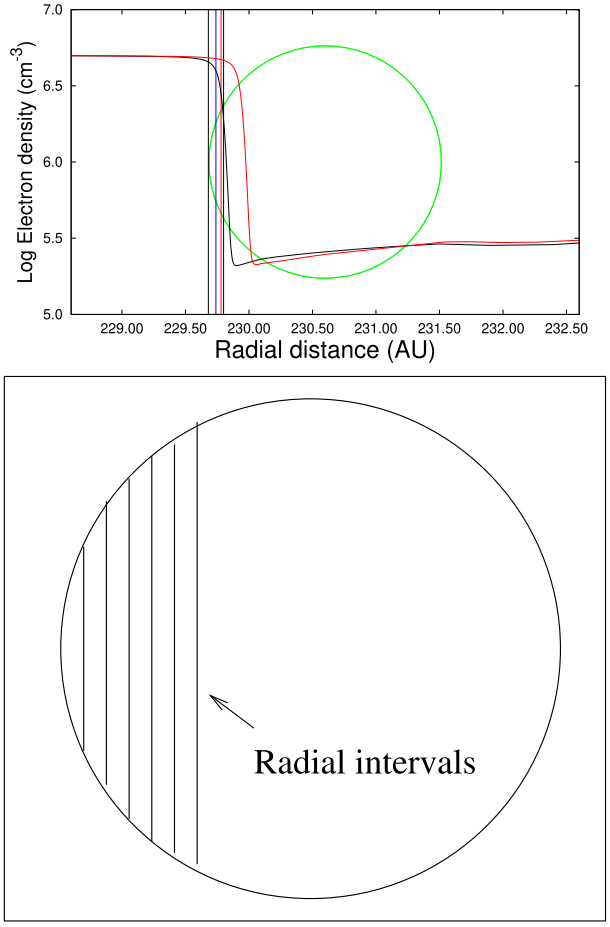

Figure 4. Top panel: the black and red lines show an example of the radially dependent electron density at the position of the IF without and with the additional SED. The circle represents the projection of the maser spot with a diameter of 2 au. The vertical lines from left to right indicate the inner edge of the maser spot at 90 per cent, 80 per cent, 60 per cent, and 40 per cent of the constant hydrogen density. Bottom panel: the vertical lines show how the maser spot is divided into equal width intervals for the calculation of the area-weighted ionization rate from the radially dependent electron density.

n_e the electron density, and n_{H_0} the neutral hydrogen density. To solve n_e(t) from equation (2), a time-dependent ionization rate (Γ(t)) has to be obtained from the equilibrium solutions of the position of the IF. An ionization rate is determined from each equilibrium solution of the position of the IF using

$$\Gamma = \frac{n_e^2 \beta}{n_{H_0}}, \tag{3}$$

from the equation of ionization balance.

Since both n_e and n_{H_0} depend on the radial distance from the central star, it follows that the ionization rate depends on the radial distance. In the CWB scenario, the maser is assumed to be a cylindrically shaped column of gas with a circular cross-section (Kylafis & Pavlakis 1999) and a diameter of 2 au (inferred from the results of Minier, Booth & Conway 2002), as illustrated in the top panel of Fig. 4. Γ is very simply obtained by the following approach. The maser spot is divided into slices of equal width as shown in the bottom panel of Fig. 4. The average electron density (area-weighted) is found by

$$\overline{n_e} = \sum_{i=1}^{n} \frac{n_{e,i} d\sigma_i}{\sum_{i=1}^{n} d\sigma_i} = \sum_{i=1}^{n} \frac{n_{e,i} d\sigma_i}{A}, \tag{4}$$

where $n_{e,i}$ is the radially dependent electron density (across the maser spot) from each interval, $d\sigma_i / \sum_{i=1}^{n} d\sigma_i$ the corresponding area-weighted contribution to the average, and $\sum_{i=1}^{n} d\sigma_i = A = \pi r^2$, the total area of the maser spot with a radius r. In the same way an average neutral density is obtained to get the Γ for each equilibrium position. The Γ's (from all the equilibrium states) are then used to construct a quasi time-dependent ionization rate, using a cubic interpolation scheme. This approach is repeated for all the sets of parameters used, which includes placing the inner edge of the projection of the maser spot at several different positions on the IF. This is shown by the vertical lines in the top panel of Fig. 4. The electron density at these positions is, respectively, 90 per cent (black line), 80 per cent (blue line), 60 per cent (red line), and 40 per cent (dashed line) of the constant neutral hydrogen density used for the CLOUDY simulations. The position of the IF in defined as the transition region where the H II region goes from fully ionized to partially ionized, and the edge of the H II region (as shown in Fig. 3) is defined as the position of the IF-driven shock.

Each quasi time-dependent ionization rate obtained is used as input to solve for $n_e(t)$ using equation (2). The solutions of equation (2) describe the time-dependent increase (the flare as a result of the ionization 'pulse') and decrease (decay due to recombination) of the electron density.

2.6 Comparing the CWB model with the maser light curves

As discussed above, the 'full' CWB model gives the change in the electron density, n_e, at the IF as a function of time. For the case when the H II region is optically thin for free–free emission propagating outward from the IF, it follows that $I_\nu \propto n_e^2$ or for the time-dependent case that $I_\nu(t) \propto n_e^2(t)$. Although it was possible to calculate the time dependence of the surface brightness of the H II region, our complete lack of knowledge about the real amplification and position of the masing region, did not allow us to model the maser emission as such. Furthermore, the geometry of the H II region used in the calculations is a highly idealized case which almost certainly deviates from reality. To compare the calculated change in n_e^2 at the IF and the observed maser emission we therefore set $I_\nu(t) = f\, n_e^2(t)$ where the proportionality constant f takes care of all the unknown factors. The value of f is determined when the model is in its quiescent state and is discussed in Section 4.4.

To find a CWB model that most closely resemble that of the observed flux density, the decay part of the flare profiles are analysed using equation (5) as discussed in the next section. This is done to find the peak and quiescent state electron densities that describe each flare. From the derived quiescent state electron densities ($n_{e,b}$'s) and peak electron densities ($n_{e,0}$'s), the CWB model(s) with the peak and quiescent state electron densities closest to the derived values are chosen for comparison with the observed maser light curves. This is done in order to obtain a similar decay profile, and a relative amplitude (see Goedhart et al. 2003, for the definition) close to that of the observed data.

3 FLARE ANALYSIS

As mentioned above, the decay of the flare is due to the time-dependent change in the free–free emission produced from the

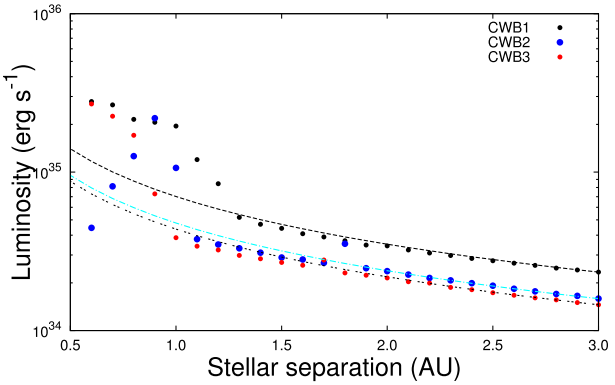

Figure 5. The luminosity of the shocked gas as a function of stellar separation distance for the three models CWB1(black points), CWB2 (blue points), and CWB3 (red points) given in Table 1. Also shown is the relation $L_{\rm shock} \propto D^{-1}$ for the three models normalized at 3.0 au.

recombination of a partially ionized gas. Thus, we apply

$$n_{\rm e}^2(t) = n_{\rm e,b}^2 \left(\frac{u_0 + \tanh(\beta n_{\rm e,b} t)}{1 + u_0 \tanh(\beta n_{\rm e,b} t)} \right)^2, \quad (5)$$

(see appendix A of van der Walt et al. 2009, for more details) to obtain the quiescent and peak electron densities. $n_{\rm e,\,b}$ is the quiescent state electron density to which the flares recombine, and $u_0 = n_{\rm e,\,0}/n_{\rm e,\,b} > 1$, with $n_{\rm e,\,0}$ the peak electron density from where recombination commence. Equation (5) is applied to each of the individual flares in G9.62 + 0.20E and G22.357 + 0.066, and the peak and quiescent electron densities associated with each flare were obtained. This is also done with the ephemeris folded data of G37.55 + 0.20 and G45.473 + 0.134 to show the general behaviour of the flares. The fit is done using a non-linear least-squares Marquardt–Levenberg algorithm. In this case, for the initial conditions we choose $n_{\rm e,\,b} = 2 \times 10^5$ cm^{-3} and $u_0 = 2$ as first guess, similar to the approach used by van der Walt (2011).

4 RESULTS

As already noted above, the full CWB model consists of a number of components. Before presenting the final results from combining all these components, we first present some results related to some of the individual components. Understanding the behaviour of the components results in a better understanding of the behaviour of the 'full' model.

4.1 Emission and SEDs produced from the shocked gas

Fig. 5 shows the dependence of the total luminosity of the shocked gas as a function of the stellar separation for the three models CWB1, CWB2, and CWB3. When the gas cools adiabatically the luminosity varies like D^{-1}, where $L_{\rm shock} \simeq \dot{M}^2 v^{-3} D^{-1}$ (Stevens et al. 1992). To examine to what extent the gas cools adiabatically in the model calculations, a D^{-1} relation is also shown in Fig. 5 for each of the three models. In each case, the D^{-1} relation was normalized to the model result at 3 au. It is seen that for all three models, the shocked gas cools adiabatically for stellar separations greater than about 1.25 au. For separations less than 1.25 au, the gas cools radiatively and the luminosity is significantly larger than what would be expected if it cools adiabatically. In the case of model CWB2, the luminosity decreases for stellar separations smaller than

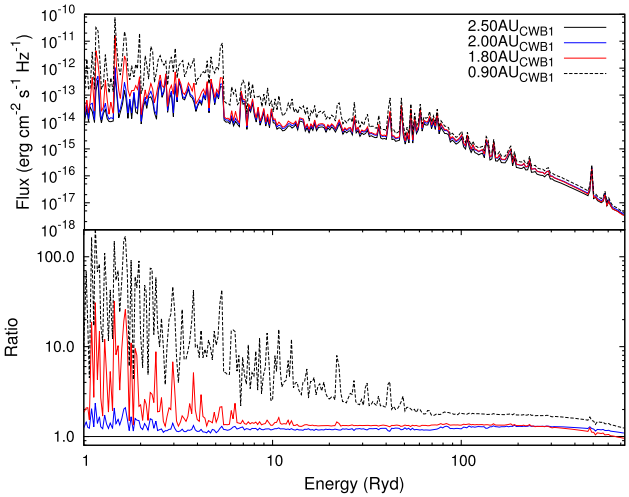

Figure 6. Top panel: results from the calculation of the SED from the shocked gas for adiabatic and radiative cooling gas. Bottom panel: the ratio of each SED relative to the SED for 2.5 au (black line). This shows that radiative cooling gas results in SEDs with increased flux of lower energy ionizing photons.

0.9 au, because radiative cooling has caused the gas to collapse into a thin cold shell.

In the adiabatic case, the shocked gas has a maximum luminosity of lg $L_{\rm shock}$(erg s^{-1}) = 34.71 at 1.3 au for model CWB1. On the other hand, if the shocked gas is dominated by radiative cooling, the luminosity increases and reaches average values of lg $L_{\rm shock}$ = 35.45 (CWB1, at 0.6 au), lg $L_{\rm shock}$ = 35.31 (CWB2, at 0.9 au), and log $L_{\rm shock}$ = 35.43 (CWB3, at 0.6 au). Interestingly, note that $L_{\rm shock} < L_{\rm wind} \ll L_\star$, with lg $L_{\rm wind}$ = 36.07 (CWB1) and lg $L_\star \simeq 38.5$. The above results confirm, as expected, that the luminosity produced from the shocked gas will only be a fraction of the wind kinetic luminosity, ie. $L_{\rm shock} \simeq \frac{1}{2}\Xi \dot{M} v^2$, where Ξ is the fraction of the kinetic luminosity normal to the contact discontinuity as defined by Pittard & Stevens (2002), and has typical values of 0.3–0.6. Thus, the luminosity produced from the shocked gas is only a small fraction of the bolometric luminosity of the star, $L_{\rm shock} \leq 10^{-3} L_\star$.

Within the framework of the CWB model, a 'pulse' of ionizing radiation is produced by the shocked gas around the periastron passage of the secondary star. It is also instructive to investigate the changes, if any, of the SED of the ionizing radiation emitted by the shocked gas for various separations of the two stars. In the upper panel of Fig. 6, we show the SEDs for model CWB1 for four stellar separations and in the lower panel the ratio of the SED's with respect to the SED for 2.5 au. The important point to note here is that the lower energy photon flux increases dramatically (more than 10-fold) for small separations (around periastron for an eccentric orbit), ie. for the case of radiative cooling of the shocked gas. Since the ionization cross-section for hydrogen is largest for the lower energy ionizing photons, this dramatic increase in the flux of ionizing photons around periastron passage suggests that it might have an effect on the IF.

4.2 CLOUDY calculations

Fig. 7 shows the results of the CLOUDY simulations when the emission from the shocked gas is added to that of the star. This shows the influence of the ionizing photons from the shocked gas at the IF, both for adiabatically – and radiatively cooling gas for

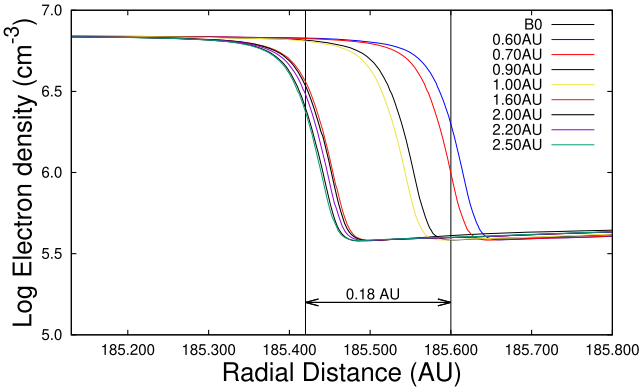

Figure 7. The resulting positions of the IF for the BB spectrum of a B0 star (black line) and several different SEDs from the shocked gas. For the larger separation distances (adiabatic SEDs), the IF does not change its position much, however, small separation distances (radiative SEDs) influence the position of the IF considerably (up to ≃0.18 au). These results are from the model CWB1.

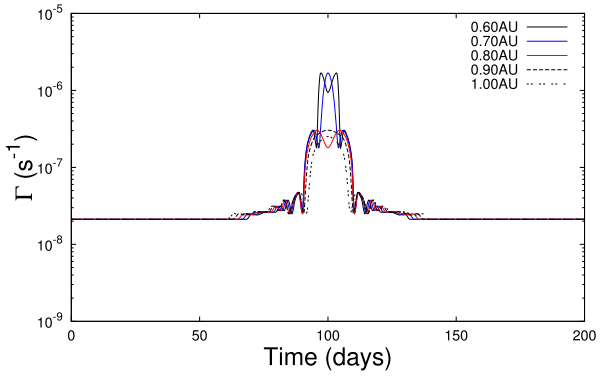

Figure 8. The interpolated time-dependent ionization rates obtained from the equilibrium states of the IF of the H II region. This is an example for a 200-d period for a fixed constant neutral hydrogen density and mass-loss rate combination, for several periastron distances.

model CWB1. It is seen that the ionizing photons produced from shocked gas cooling adiabatically (1.6–2.5 au and beyond) cause minimal changes ($\leq 10^{11}$ cm, $\leq$ 0.006 au) in the position of the IF. In comparison, the ionizing photons produced from the shocked gas cooling radiatively (0.6–1.0 au) has an increased effect (up to $\approx 2.7 \times 10^{12}$ cm, 0.18 au) at the IF. This difference is due to the increased emission of lower energy ionizing photons above the hydrogen ionization threshold, when the shocked gas cools radiatively. These results strongly suggest that the emission produced from the radiatively cooling shocked gas around periastron is sufficient to cause changes at the IF. Subsequently a 'small' separation distance, at periastron passage, is necessary to cause a significant outward shift of the IF in order to explain the flare profiles as a result of the time-dependent change in the free–free emission. This strongly suggests that an eccentric orbit, as originally proposed by van der Walt (2011), is necessary to explain the periodicity as a result of a CWB system.

4.3 Time dependence of free–free emission

Using the approach described in Section 2.5, the ionization rates were calculated at the IF for each equilibrium position (i.e. for each SED of every stellar separation) of the IF obtained using model CWB1. The quasi time-dependent ionization rate was then constructed by using apastron as the start of an orbit and interpolating. Fig. 8 shows examples of the time-dependent ionization rates calculated from the equilibrium states. These examples show several periastron distances, for a fixed hydrogen density and a fixed position of the maser spot on the IF. The increase in the ionization rate represents the 'pulse' of additional ionization at the IF during periastron passage. One thing that has to be kept in mind is that due to the averaging of the SEDs of several 'snapshots', the resulting influence at the IF may not necessarily change linearly with luminosity. Radiative cooling effects may cause different influences at the IF for different SEDs, and the time-dependent ionization rate at the IF may not be smooth as seen in Fig. 8.

4.4 Flare and time-series analysis

Before comparing the results of the 'full' CWB model with the observed time series, it is instructive to first analyse the individual flares of G9.62 + 0.20E and G22.357 + 0.066 by fitting equation (5) to the decay parts of the flares. This allows us to estimate electron densities at the peak of a flare as well as during the quiescent state.

This was also done for the ephemeris folded data of G37.55 + 0.20 and G45.473 + 0.134, which resulted in one peak and one quiescent state value. Fig. 9 shows, from top to bottom, examples of the fit of equation (5) to flare 13 of G9.62 + 0.20E, flare 2 of G22.357 + 0.066 (see Table 2), and a fit to the ephemeris folded profiles of G37.55 + 0.20 and G45.473 + 0.134. It is seen that in all four cases the decay of the flare is described very well by the decrease of the free–free emission due to the recombination of a partially ionized hydrogen plasma from a higher to a lower state of ionization. Table 2 summarizes the results of fitting equation (5) to 13 flares of G9.62 + 0.20E, six flares of G22.357 + 0.066, as well as for the ephemeris folded data of G37.55 + 0.20 and G45.473 + 0.134. For G37.55 + 0.20, both methanol (CH_3OH) and formaldehyde (H_2CO) were used. The average peak and quiescent state electron densities of all the sources are remarkably similar, with values $(1.13 \pm 0.20) \times 10^6$ cm^{-3} and $(5.6 \pm 0.8) \times 10^5$ cm^{-3} for G9.62 + 0.20E, $(1.08 \pm 0.16) \times 10^6$ cm^{-3} and $(6.7 \pm 1.1) \times 10^5$ cm^{-3} for G22.357 + 0.066, $(1.11 \pm 0.22) \times 10^6$ cm^{-3} and $(4.0 \pm 1.5) \times 10^5$ cm^{-3} for G37.55 + 0.20 and $(1.22 \pm 0.11) \times 10^6$ cm^{-3} and $(4.6 \pm 0.8) \times 10^5$ cm^{-3} for G45.473 + 0.134.

From the quality of the recombination fits to the decay profiles of the flares, the assumption that the H II region is optically thin (ie. $I_\nu \propto n_e^2$) from the IF towards the masers is probably correct. Visual inspection of the maser light curve of G9.62 + 0.20E shows that the observed quiescent state and peak flux densities increases with time, as seen in the top panel of Fig. 10. To test if this is the case for the $n_{e,b}^2$'s and $n_{e,0}^2$'s, which is summarized in Table 2, the bottom panel of Fig. 10 shows the $n_{e,b}^2$'s and $n_{e,0}^2$'s for each flare of G9.62 + 0.20E. It also shows a linear regression to both the $n_{e,b}^2$'s and the $n_{e,0}^2$'s. Both the $n_{e,b}^2$'s and $n_{e,0}^2$'s is seen to increase with time, similar to the observed flux density. The expressions for the time-dependent behaviour of the quiescent and peak electron densities associated with the flares are:

$$n_{e,b}^2 = (3.30 \pm 2.54) \times 10^7 t + (1.78 \pm 0.47) \times 10^{11}, \quad (6)$$

$$n_{e,0}^2 = (2.52 \pm 1.22) \times 10^8 t + (5.44 \pm 1.96) \times 10^{11}. \quad (7)$$

In order to compare these expressions with the observed flux density, a linear regression fit is applied to the time-dependent quiescent

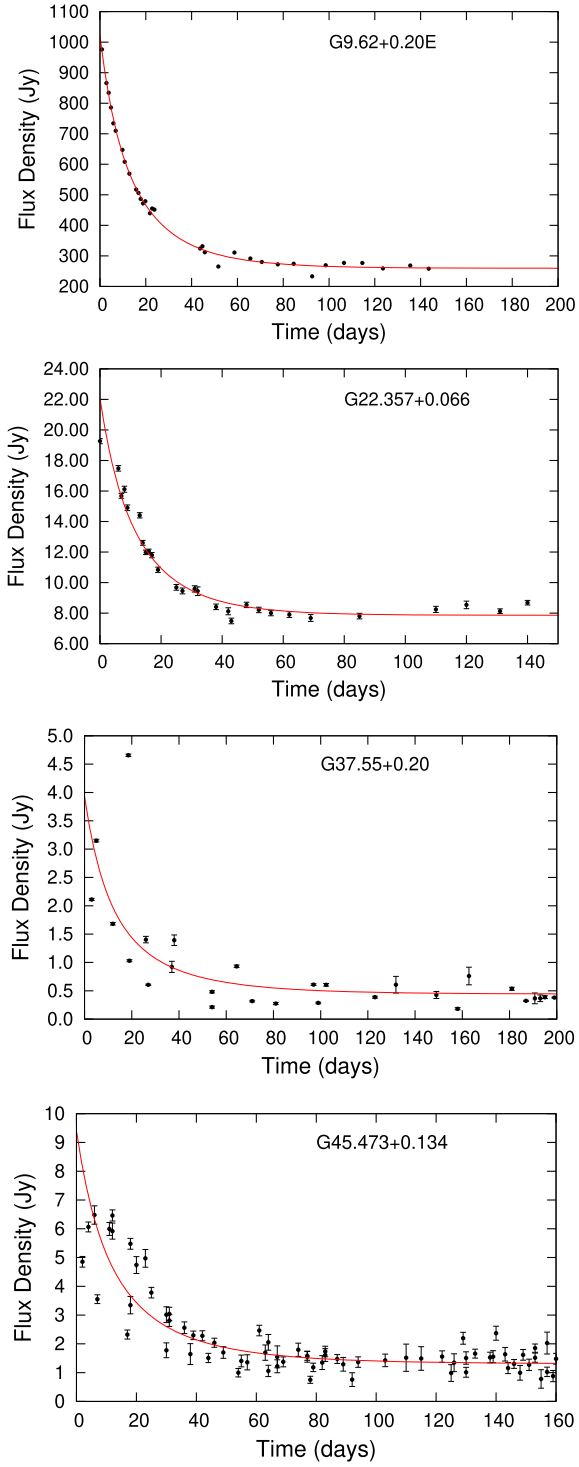

Figure 9. Example fits of equation (5) to a flare of G9.62 + 0.20E, G22.357 + 0.066, and the ephemeris folded data of G37.55 + 0.20 and G45.473 + 0.134.

state flux density. The gradient obtained for the time-dependent quiescent state flux density is 0.027 ± 0.001 Jy d^{-1}. To compare $n^2_{\rm e,b}(t)$ with the observed flux density, we use MJD 55000 (indicated by 'x' in the top panel of Fig. 10), and divide equation (7) by the factor $\sim$1.25 × 10$^9 n_{\rm e}^2$ Jy^{-1}, which puts $n^2_{\rm e}(t)$ at the level of the observed flux density and we find the gradient of equation (7) as 0.026 ± 0.020 Jy d^{-1}. The blue line in the top panel of Fig. 10 represents the linear regression of the quiescent state flux density, and the red dashed line in the top panel (which follows the blue line closely) represents the scaled linear regression of $n^2_{\rm e,b}(t)$. The agreement between these two independent methods suggests that the observed quiescent state flux density follows the time-dependent change in $n^2_{\rm e}$ from the background H II region. Additionally, the top panel of Fig. 10 shows the time-dependent behaviour of $n^2_{\rm e,0}$ (black line). This was after equation (6) was scaled to flux density assuming a relative amplitude of 2.2 (Goedhart et al. 2003) at MJD 55000. This means that the black line in the top panel of 10 will have a value for the peak flux density or $n^2_{\rm e,0}$ such that the relative amplitude will be 2.2 at MJD 55000, for the quiescent state flux density or the quiescent state electron density at 'x', given the definition of relative amplitude, $R = \frac{S_{\rm p}-S_{\rm q}}{S_{\rm q}} = \frac{n^2_{\rm e,0}-n^2_{\rm e,b}}{n^2_{\rm e,b}}$, where $S_{\rm p}$ and $S_{\rm q}$ is the peak and quiescent flux density, respectively. The gradient of $n^2_{\rm e,0}(t)$ is obtained as 0.20 ± 0.10 Jy d^{-1}. This also describes the observed trend of the time-dependent increase of the maximum flux density with time as due to a time-dependent increase in $n_{\rm e,0}$.

Similarly, applying a linear regression to $n^2_{\rm e,b}(t)$, $n^2_{\rm e,0}(t)$, and the quiescent state flux density of G22.357 + 0.066, we obtained the results shown in Fig. 11. The bottom panel again shows the linear regression fits to $n^2_{\rm e,0}(t)$ and $n^2_{\rm e,b}(t)$. The blue line in the top panel shows the linear regression fit to the quiescent state flux density, and the red line shows the linear regression fit of $n^2_{\rm e,b}(t)$ scaled to the quiescent state flux density by the factor 4.5 × 10^{10} $n_{\rm e}^2$ Jy^{-1} at MJD 55800. The gradient of the linear regression fit to the quiescent state

Table 2. The individual periodic maser sources with their associated periods (in days, given in brackets). For each source, each flare is given at its associated time at the peak of the flare using MJD convention, together with the corresponding quiescent and peak electron density from the recombination curve fits. The periods are obtained from e.g. Goedhart et al. (2003). Araya et al. (2010), Szymczak et al. (2011), and Szymczak et al. (2015).

Flare (MJD) G9.62 + 0.20E (244)	Peak $n_{\rm e,\star}$ (× 10^6 cm^{-3})	Quiescent $n_{\rm e,b}$ (× 10^5 cm^{-3})
53187	1.24 ± 0.10	6.9 ± 0.5
53429	1.00 ± 0.11	5.2 ± 0.5
53670	0.92 ± 0.07	5.3 ± 0.4
53919	1.15 ± 0.07	6.3 ± 0.4
54159	0.79 ± 0.04	4.1 ± 0.2
54407	0.87 ± 0.04	4.3 ± 0.2
54645	1.34 ± 0.15	5.8 ± 0.6
55627	1.20 ± 0.09	5.4 ± 0.4
55863	1.17 ± 0.18	6.8 ± 0.9
56109	1.25 ± 0.11	6.0 ± 0.5
56347	1.16 ± 0.07	5.5 ± 0.3
56591	1.49 ± 0.10	5.6 ± 0.3
56835	1.20 ± 0.09	5.7 ± 0.3
G22.357 + 0.066 (179)		
55529	1.18 ± 0.02	8.2 ± 0.8
55718	1.28 ± 0.03	7.7 ± 0.7
55886	1.23 ± 0.04	6.9 ± 0.8
56060	0.99 ± 0.02	6.0 ± 0.6
56244	0.93 ± 0.02	6.4 ± 1.1
56603	0.91 ± 0.02	5.3 ± 0.5
G37.55 + 0.20 (237)		
CH_3OH	1.13 ± 0.26	3.8 ± 1.4
H_2CO	1.08 ± 0.17	4.1 ± 1.6
G45.473 + 0.134 (196)		
CH_3OH	1.22 ± 0.11	4.6 ± 0.8

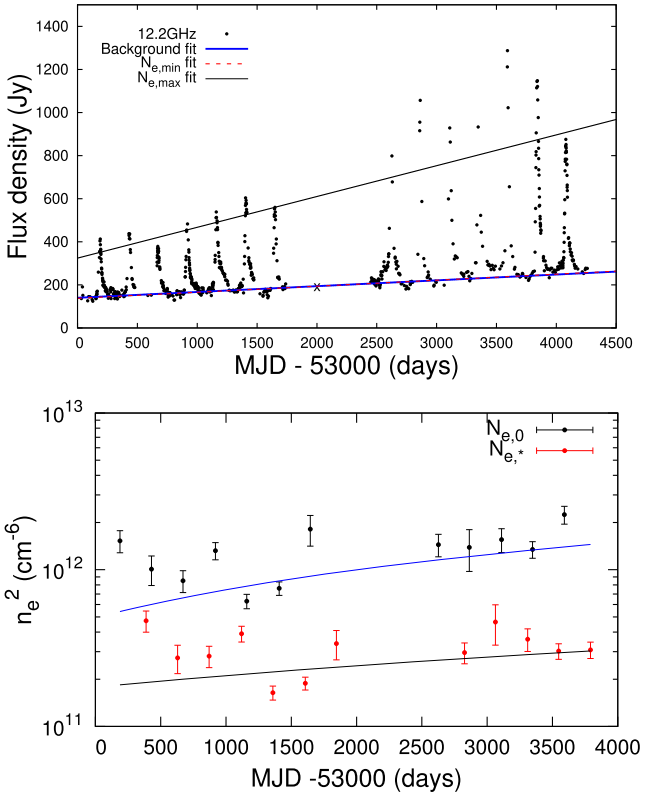

Figure 10. Top panel: the best linear regression fit (blue line) to the quiescent flux density of the maser overlaid with the normalized best linear regression fit to the time-dependent $n^2_{e,b}$ values (red dashed line), as well as a normalized fit to the $n^2_{e,0}$ values with relative amplitude of $\simeq$2.2 (black line). Note that the n^2_e's is on a logarithmic scale. Bottom panel: the quiescent and peak electron densities as a function of time are shown as determined by the recombination fits of G9.62 + 0.20E.

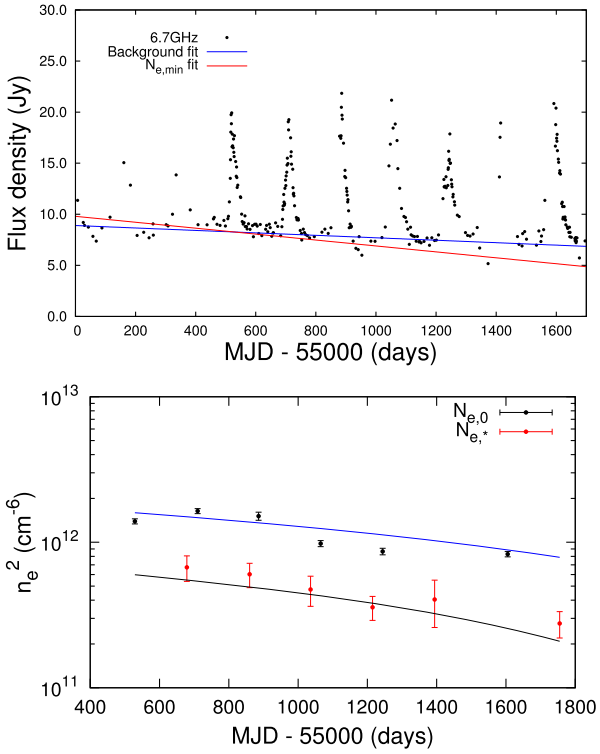

Figure 11. Top panel: the fitted gradient of the regression fit to the quiescent state flux density for G22.357 + 0.066 (blue line), as well as the fitted gradient of the $n^2_{e,b}$ values (red line). Note that the n^2_e's is on a logarithmic scale. Bottom panel: the quiescent and peak electron densities as a function of time are shown as determined by the recombination fits of G22.357 + 0.066.

flux density (blue line) is -0.0010 ± 0.0002 Jy d^{-1}, and the gradient of $n^2_{e,b}(t)$ after scaling it is -0.0030 ± 0.0015 Jy d^{-1}. Although the gradients are not exactly the same, with the error margin the smallest gradient for $n^2_{e,b}(t)$ is close to that obtained for the quiescent state flux density. This also suggests that the observed quiescent state flux density might be due to a time-dependence of n^2_e. It is important to know that in obtaining the linear regression fits to the $n^2_{e,b}(t)$'s and $n^2_{e,0}(t)$'s both for G9.62 + 0.20E and G22.357 + 0.066, each point was weighted by its error margins.

4.5 Comparison of CWB model with maser light curve

To compare the CWB model with the observed flux densities for G9.62 + 0.20E and G22.357 + 0.066, $n^2_{e,b}(t)$ is scaled to the quiescent flux density as discussed in Section 2.6. Additionally, the gradients of $n^2_{e,b}(t)$ for G9.62 + 0.20E and G22.357 + 0.066 were also artificially incorporated for the comparisons. Although, it might be possible to compare the parameters used to obtain a CWB model solution with physical parameters estimated from observations for these sources, it might not be realistic. For this reason, CWB model solutions are chosen on the basis that the quiescent state electron density of the solutions closely compares with the derived values from the recombination fits. Thus, to be purely chosen on the basis that the solutions follow the time-dependent free–free emission from an optically thin IF. This means the CWB model solutions with $n_{e,b}$ closest to the derived values are chosen, as well as with peak values which results in a relative amplitude (see Goedhart et al. 2003, for definition) that is comparable with the relative amplitude of the observed flux density.

The upper panel of Fig. 12 shows the comparisons of the light curves of CWB models 1 and 2 (in Table 3) with the observed light curve of G9.62 + 0.20E from MJD 53000−54800. The bottom panel shows the comparisons of the light curves of the CWB models 3 and 4 with the observed light curve from MJD 55500−58000. The Hartebeeshoek Radio Astronomy Observatory 26-m telescope was being repaired during the time from MJD 54800−55500. It is seen in Fig. 12 that the peak flux density of G9.62 + 0.20E has increased significantly after the telescope was repaired. Instrumental effects as the cause of the increase have been ruled out, implying the source brightness has actually increased. For this reason, the comparison of the CWB model with the two data sets was done separately. The parameters used to obtain these comparisons are summarized in Table 3. Table 3 gives, in order from left to right, the model, the spectral type of the primary star, the peak and quiescent electron densities associated with each CWB model, the periastron distance for the binary orbit, its subsequent eccentricity for the given period and fixed total system mass of 38 $M_\odot$, the hydrogen density used to simulate the H II region, and the position where the maser spot was placed on the IF. All of these results were obtained using a maser spot diameter of 2 au and the model CWB1 from Table 1 was used for all the fits.

The light curves from the CWB models compare very well with the observed time-dependent flux density of G9.62 + 0.20E. For instance, models 1 and 3 compare very well with both the observed light curves before and after the 'gap' in the data. However, note

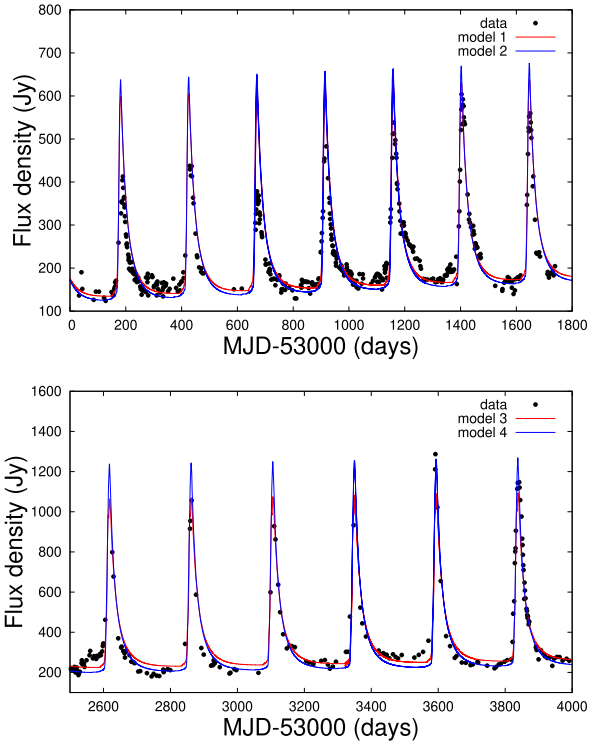

Figure 12. Top panel: comparisons of models 1 and 2 from Table 3 with the observed maser light curves of G9.62 + 0.20E from MJD 53000 to 54800. Bottom panel: comparisons of models 3 and 4 from Table 3 with the observed maser light curves of G9.62 + 0.20E from MJD 55500 to 58000.

that the orbital configuration of the binary system changed using these two comparisons. It is important to see, however, that given that the time-dependence of the electron density depends on the position of the maser spot on the IF, it is rather the idea that the position of the IF has changed from before to after the 'gap' in the data. This is based on the most probable case that for an Ultra compact HII (UCHII) region, which G9.62 + 0.20E is (Hofner et al. 1996; Sanna et al. 2015), the IF is probably still expanding towards pressure equilibrium. Thus, it is not that the eccentricity of the binary system changed but, that a solution was chosen that provides for the time-dependent increase in both the quiescent and peak electron densities after the 'gap'.

The parameters used for the comparison of CWB model 1 (blue line) and CWB model 2 (red line) in Fig. 13 with the maser light curve of G22.357 + 0.066 are also summarized in Table 3. Similarly two CWB models were compared to the ephemeris folded data of G37.55 + 0.20 and G45.473 + 0.134, because the data sampling was too sparse to compare the CWB model with these maser light curves. These models are also summarized in Table 3.

In principle to obtain a best 'fit' CWB model, a minimal χ^2 fit should be done. However, given that the 'full' CWB model consists of four components and uses a complex multiparameter approach (which led to the use of discrete points from parameter space), it would be difficult to apply a χ^2 fit. Therefore, it was decided not to apply a χ^2 fit.

5 DISCUSSION

In Sanna et al. (2015), the maser positions for G9.62 + 0.20E are shown relative to the 7 mm continuum peak of the UCHII region. It shows that the masers are projected close to the edge of the peak of the continuum. From the quality of the comparison of the CWB model with the observed maser light curves, and the agreement between the derived time-dependent quiescent state electron density and the time-dependent quiescent state flux density, it is reasonable to conclude that the flaring of the periodic methanol masers in G9.62+0.20E and G22.357 + 0.066 are likely to be due to a time-dependent change in the free–free emission from the background UCHII region. The maser spots, exhibiting these periodic variations, are then probably projected against some small volume of partially ionized gas that changes its state of ionization time-dependently due to some ionization event.

Consider now the likely case that the UCHII region expands in an inhomogeneous and clumpy environment (see e.g. Viti 2003; Indebetouw et al. 2006). The masers can either probe a clump or the IF of the UCHII region. Assuming that the radial-dependent electron density of the UCHII region resembles that of the results from the CLOUDY simulations, a clump should reside within the fully ionized gas of the H II region. This is because, if the clump was located to the outside of the IF, most of the ionizing photons will effectively be absorbed at the IF and the clump will be isolated from the ionizing radiation, and if the clump were to coincide with the IF it will make no difference to the radially dependent structure at the IF, the electron density will only scale with density. However, in the case where the clump resides inside of the IF in the fully ionized gas, the ionizing photons will be absorbed by the clump first. This, however, might probably not explain the periodic variations, because our calculations show that the UCHII region is optically thick at 6.7 and 12.2 GHz, and no variations of the free–free emission from the clump will be 'visible' to the outside of the IF. It will thus be difficult to envision that the time-dependence of the free–free emission from the clump could explain the periodic variations of the masers. On the other hand, the H II region, from the IF outward, is optically thin and the increase and subsequent decrease in the free–free emission from the IF will resemble the time-dependence of the electron density, and should be detectable by the maser. This makes the IF the most likely region to be the source of the variations in the free–free emission. It is certainly true that the question can be raised about the probability that the maser spots are projected favourably against the IF of the H II region? In this regard, it can be argued that statistically we are simply observing these sources at a favourable time during the evolution of the UCHII region such that the masers are 'now' projected against the outward moving IF. This might also explain the small number statistics of periodic methanol masers.

On the other hand, Szymczak et al. (2015) favour the models proposed by Araya et al. (2010) and Parfenov & Sobolev (2014) for the flaring of G22.357 + 0.066. These authors argue that since the variability index of individual maser features are different, the CWB model will not be able to explain the different profiles. However, since the UCHII region is likely expanding inside an inhomogeneous molecular cloud, such that individual masers probe different density structures, equation (5) indicates that different density structures should result in different flare profiles. This means that although different velocity features show different flare profiles, the CWB model will still be able to explain the different flare profiles within the same source.

With the framework that the masers probe the time-dependent change in the free–free emission from the IF of the UCHII region, the time-dependent increase of the quiescent state flux density of G9.62 + 0.20E is proposed to be a result of the expansion of the IF across the line of sight of the maser spot. Given that we are investigating HMSFRs, the best-case scenario is that the UCHII

Table 3. A summary of the CWB models. The spectral type of the primary star, and the quiescent and peak electron densities are noted in columns 2−4. The remaining columns note the periastron distance used for the orbit, the eccentricity (ϵ) of the orbit, the hydrogen density used to simulate the H II region, and lastly the position where the maser spot was placed on the IF (as apercentage of the constant hydrogen density) as described in Section 2.

Model G9.62 + 0.20E (244)	Spectral type	Peak $n_{e,0}$ ($\times 10^6$ cm^{-3})	Quiescent $n_{e,b}$ ($\times 10^5$ cm^{-3})	Periastron (au)	Eccentricity (e)	n_{H^0} ($\times 10^6$ cm^{-3})	Maser position (per cent)
1	B0	1.21	5.6	0.9	0.65	5	80
2	B0	1.25	5.4	1.0	0.61	7	60
3	B0	1.40	5.6	0.7	0.73	5	80
4	B0	1.60	5.4	0.9	0.65	7	60
G22.357 + 0.066 (179)							
1	O9	1.05	6.4	1.0	0.52	7	60
2	O9	1.25	6.4	0.9	0.57	7	60
G37.55 + 0.20 (237)							
1	B0	1.30	4.4	0.8	0.64	6	60
2	B0	1.38	4.4	0.9	0.56	6	60
G45.473 + 0.134 (196)							
1	B0	1.26	5.57	1.0	0.55	7	60
2	B0	1.32	4.6	0.9	0.59	6	60

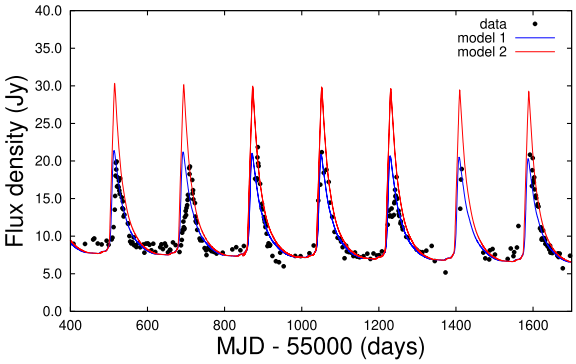

Figure 13. A comparison of CWB models 1 and 2 (see Table 3) with the observed maser light curve for G22.357 + 0.066 from MJD 55400 to 56700.

region (maintained by the primary star) has reached its initial Strömgren radius, but is not yet in pressure equilibrium with its surrounding molecular cloud. It is then reasonable to assume that the IF is still expanding towards pressure equilibrium, and the expansion of the IF across the line of sight passing through the maser spot can explain the time-dependent increase of the quiescent state free–free emission from the IF of the background UCHII region. There is also the distinct possibility that, not only does the IF expand, but the maser spot might also not be stationary (Day et al. 2010; Xu et al. 2012; Asaki et al. 2014; Bartkiewicz, Szymczak & van Langevelde 2014), and it might be the relative motion between the maser spot and the IF that causes the possible decrease in the free–free emission of G22.357 + 0.066.

Before we determine the velocity of the IF it is necessary to state the twofold dilemma caused by the static equilibrium positions of the IF and the solution of the time-dependent electron density. This twofold dilemma is that from the static equilibrium solution of the CLOUDY calculation we obtain the steady-state radially dependent electron density but no time-dependent information, whereas, the time-dependent solution provide us with time-dependent information on the ionization rate at the IF but no radially dependent electron density information. Although we have this dilemma, the quality of the comparison of the quasi time-dependent CWB model with the observed maser light curve, suggests that it is still a reasonably accurate representation of the full time-dependence. Thus, using the area-weighted approach to calculate the average electron density across the maser spot, and the derived time-dependent electron density from the recombination fits of the flares, it is possible to estimate the expansion velocity of the IF. First, we choose two electron densities from the linear regression fit of equation (6), in this case it is done at MJD 54000 and 56000. Second, using the area-weighted approach it is determined by how much the IF must shift to achieve these two electron densities. From the shift and the time difference, the velocity of the IF is determined as $\simeq$50 m s^{-1}.

Although this approach may be simplistic, this result may have important implications, and might explain the H II region lifetime problem discussed by Wood & Churchwell (1989), de Pree, Rodriguez & Goss (1995), and Churchwell (2002). According to these authors, there are more UCHII regions observed than expected from a standard star formation rate and the initial mass function. The expected number of UCHII regions was derived for a constant expansion velocity of $\simeq$10 km s^{-1} for the IF, which is the sound speed in the ionized gas as the H II region reaches the Strömgren radius. Akeson & Carlstrom (1996) performed numerical calculations which showed that the IF velocity slows down to $\simeq$1 km $^{-1}$ after $\approx 3 \times 10^4$ yr to as low as 0.1 km s^{-1} after $\approx 10^5$ yr (after the initial Strömgren radius has been reached) for a constant neutral hydrogen density of $\sim 10^6$ cm^{-3}. These values also depend on the ambient density and temperature (Wood & Churchwell 1989), and might even be lower than this for a denser and warmer ambient medium. In the case of G9.62 + 0.20E, the density is $\simeq 10^7$ cm^{-3} with a dust temperature of $\simeq$100 K (Hofner et al. 1996), which could explain such a low-derived velocity of the IF.

Given the idea that the IF is expanding across the line of sight passing through the maser spot, this velocity at which the IF might be expanding could also explain why the periodicity has been so stable. For the case where the IF expands at the speed of sound in the ionized gas ($\sim$10 km s^{-1}), the IF would have expanded across the line of sight of the maser (for a diameter of 2 au) in $\sim$1 yr, after which the periodicity would have disappeared. On the other hand, if the IF is expanding at lower velocities, such as the derived

value of $\sim 50\,\mathrm{m\,s^{-1}}$, the periodicity in G9.62 + 0.20E is predicted to persist for up to 200 yr. In reality, this might be oversimplified and it is likely a combined effect of both the expansion of the IF and the motion and projection of the maser spot on the IF. Thus, in reality, the IF might expand at a different velocity than derived, but due to projection effects relative to the maser result in the derived velocity. Lastly, in either of these cases, if the periodicity is indeed due to the time-dependent change of the free–free emission from the IF (due to a CWB system) the periodicity will switch-on when the maser starts to 'see' the IF and switch-off when the IF has expanded across the line of sight of the maser. With this said, we would be able to predict the evolution of the flare profile to the point where the periodicity disappears and continually test the hypothesis.

The original paper of van der Walt (2011) only addressed some general aspects of the CWB scenario. The toy model assumed that the shocked gas cools adiabatically through the entire orbit, ie. $L \propto 1/D$, with the additional assumption that the radiation emitted from the shocked gas is sufficient to influence the position of the IF. Although the toy model describes the flare profile rather well, the assumption of $L \propto 1/D$ required a highly eccentric ($e \approx 0.9$) binary orbit. In this work, where the effect of radiative cooling was taken into account, the shocked gas was found to cool radiatively for small separations (<1.3 au) between the two stars. For the period of G9.62 + 0.20E, and the total system mass of $38\,\mathrm{M_\odot}$ (as assumed in Section 2), the shocked gas will cool radiatively for eccentricities ≥0.5 obtained from *Kepler*'s laws. Thus, the assumption of van der Walt (2011) that the shocked gas only cools adiabatically for the entire orbit was most probably not correct. When the shocked gas cools radiatively the flux of lower energy ionizing photons, where the ionization cross-section for HI is the largest, increases dramatically. This is shown to cause considerable changes in the position of the IF, which strongly suggests that the emission produced from the shocked gas is energetically feasible to cause changes in the position of the IF. This indicates that the original requirement of a highly eccentric orbit for the model of van der Walt (2011) is significantly relaxed.

From the quality of the comparison of the CWB model with the observed maser light curves, which is shown in Figs 12 and 13, and the agreement between the derived time-dependent quiescent state electron and the flux densities, it is reasonable to conclude that the flaring of the periodic methanol masers in G9.62 + 0.20E and G22.357 + 0.066 is likely to be due to the time-dependent change in the free–free emission from the background H II region against which the masers are proposed to be projected.

6 CONCLUSIONS

Considering the above result, we conclude that the CWB model can explain the periodic methanol masers. In the case of G9.62+0.20E, the CWB model reproduces the flare profiles of the 12.2 GHz periodic methanol maser over a period of 4000 d very well. The CWB model also describes the flare profiles of the 6.7 GHz methanol maser in G22.357 + 0.066 over 1600 d, as well as the average flare profiles of G37.55 + 0.20 (both methanol and formaldehyde) and G45.473 + 0.134 very well. The fact that it is possible to explain the flare profiles of several individual sources with the CWB model, as well as different masing species, strongly suggests a common driving mechanism such as a CWB system. With this hypothesis, the estimated lifetime of the periodic variations is expected to be ≈200 yr. In addition, we will be able to continually test this given the assumption that the periodicity switches-on and off as the maser's projection against the IF changes with time.

The quality of the comparison of the CWB model with the methanol masers should give merit to establish whether there are binary systems present in these HMSFRs. Thus, it is worthwhile to observe these source in the X-ray to test the hypothesis.

ACKNOWLEDGEMENTS

Stefanus Petrus van den Heever (SPvdH) want to thank Sharmila Goedhart and Jabulani Maswanganye as well as Mike Gaylard (aposthumously) for the collection and provision of the data of G9.62 + 0.20E presented. SPvdH also like to thank M. Szymczak and E. Araya for the data of G22.357 + 0.066, G37.55 + 0.20, and G45.473 + 0.134. This work is based on the research supported in part by the National Research Foundation of South Africa under the grant 96244, and also in part through the Square Kilometer Array project under the grant 79045. Any opinion, finding and conclusion or recommendation expressed in this material is that of the author(s) and the NRF does not accept any liability in this regard. The author(s) would like to thank the anonymous referee(s) for the constructive comments.

REFERENCES

Akeson R. L., Carlstrom J. E., 1996, ApJ, 470, 528
Araya E. D., Hofner P., Goss W. M., Kurtz S., Richards A. M. S., Linz H., Olmi L., Sewiło M., 2010, ApJ, 717, L133
Asaki Y., Imai H., Sobolev A. M., Parfenov S. Y., 2014, ApJ, 787, 54
Bartkiewicz A., Szymczak M., van Langevelde H. J., 2014, A&A, 564, A110
Bartkiewicz A., Szymczak M., van Langevelde H. J., Richards A. M. S., Pihlström Y. M., 2009, A&A, 502, 155
Batrla W., Matthews H. E., Menten K. M., Walmsley C. M., 1987, Nat, 326, 49
Bernabeu G., Magazzu A., Stalio R., 1989, A&A, 226, 215
Blondin J. M., Stevens I. R., 1990, BAAS, 22, 1294
Breen S. L., Caswell J. L., Ellingsen S. P., Phillips C. J., 2010, MNRAS, 406, 1487
Breen S. L., Ellingsen S. P., Contreras Y., Green J. A., Caswell J. L., Stevens J. B., Dawson J. R., Voronkov M. A., 2013, MNRAS, 435, 524
Caswell J. L. et al., 2010, MNRAS, 404, 1029
Caswell J. L. et al., 2011, MNRAS, 417, 1964
Churchwell E., 2002, ARA&A, 40, 27
Day F. M., Pihlström Y. M., Claussen M. J., Sahai R., 2010, ApJ, 713, 986
De Buizer J. M., 2003, MNRAS, 341, 277
de Pree C. G., Rodriguez L. F., Goss W. M., 1995, RevMexAA, 31, 39
Ellingsen S. P., 2006, ApJ, 638, 241
Ferland G. J., Korista K. T., Verner D. A., Ferguson J. W., Kingdon J. B., Verner E. M., 1998, PASP, 110, 761
Fujisawa K. et al., 2014, PASJ, 66, 78
Goedhart S., Gaylard M. J., van der Walt D. J., 2003, MNRAS, 339, L33
Goedhart S., Gaylard M. J., van der Walt D. J., 2004, MNRAS, 355, 553
Goedhart S., Minier V., Gaylard M. J., van der Walt D. J., 2005, MNRAS, 356, 839
Goedhart S., Gaylard M. J., van der Walt D. J., 2007, in Astrophysical Masers and their Environments Periodic Variations in 6.7-GHz Methanol Masers, Cambridge University press
Goedhart S., Langa M. C., Gaylard M. J., van der Walt D. J., 2009, MNRAS, 398, 995
Green J. A. et al., 2010, MNRAS, 409, 913
Green J. A. et al., 2012, MNRAS, 420, 3108
Hofner P., Kurtz S., Churchwell E., Walmsley C. M., Cesaroni R., 1996, ApJ, 460, 359
Inayoshi K., Sugiyama K., Hosokawa T., Motogi K., Tanaka K. E. I., 2013, ApJ, 769, L20

Indebetouw R., Whitney B. A., Johnson K. E., Wood K., 2006, ApJ, 636, 362
Kaastra J. S., Mewe R., 2000, in Bautista M. A., Kallman T. R., Pradhan A. K., eds, Atomic Data Needs for X-ray Astronomy, p. 161
Kuiper G. P., 1938, ApJ, 88, 472
Kylafis N. D., Pavlakis K. G., 1999, in Lada C. J., Kylafis N. D., eds, NATO Advanced Science Institutes (ASI) Series C, Vol. 540, p. 553
Mason B. D., Gies D. R., Hartkopf W. I., Bagnuolo J. W. G., ten Brummelaar T., McAlister H. A., 1998, AJ, 115, 821
Maswanganye J. P., Gaylard M. J., Goedhart S., Walt D. J. v. d., Booth R. S., 2015, MNRAS, 446, 2730
Maswanganye J. P., van der Walt D. J., Goedhart S., Gaylard M. J., 2016, MNRAS, 456, 4335
Menten K. M., 1991, ApJ, 380, L75
Minier V., Booth R. S., Ellingsen S. P., Conway J. E., Pestalozzi M. R., 2000, in Conway J. E., Polatidis A. G., Booth R. S., Pihlström Y. M., eds, EVN Symp. 2000, Proc. 5th European VLBI Network Symposium. Onsala Space Observatory, Sweden, p. 179
Minier V., Booth R. S., Conway J. E., 2002, A&A, 383, 614
Norris R. P., Whiteoak J. B., Caswell J. L., Wieringa M. H., Gough R. G., 1993, ApJ, 412, 222
Panagia N., 1973, AJ, 78, 929
Parfenov S. Y., Sobolev A. M., 2014, MNRAS, 444, 620
Pittard J. M., Stevens I. R., 2002, A&A, 388, L20
Sanna A. et al., 2015, ApJ, 804, L2
Sternberg A., Hoffmann T. L., Pauldrach A. W. A., 2003, ApJ, 599, 1333
Stevens I. R., Blondin J. M., Pollock A. M. T., 1992, ApJ, 386, 265
Szymczak M., Wolak P., Bartkiewicz A., van Langevelde H. J., 2011, A&A, 531, L3
Szymczak M., Wolak P., Bartkiewicz A., 2015, MNRAS, 448, 2284
Testi L., Hofner P., Kurtz S., Rupen M., 2000, A&A, 359, L5
van der Walt D. J., 2011, AJ, 141, 152
van der Walt D. J., 2014, A&A, 562, A68
van der Walt D. J., Sobolev A. M., Butner H., 2007, A&A, 464, 1015
van der Walt D. J., Goedhart S., Gaylard M. J., 2009, MNRAS, 398, 961
van der Walt D. J., Maswanganye J. P., Etoka S., Goedhart S., van den Heever S. P., 2016, A&A, 588, A47
Vink J. S., de Koter A., Lamers H. J. G. L. M., 2000, A&A, 362, 295
Viti S., 2003, Astrophys. Space. Sci., 285, 791
Wood D. O. S., Churchwell E., 1989, ApJS, 69, 831
Xu Y. et al., 2012, in Booth R. S., Vlemmings W. H. T., Humphreys E. M. L., eds, IAU Symp. Vol. 287, Cosmic Masers - From OH to H0. Kluwer, Dordrecht, p. 368

This paper has been typeset from a TEX/LATEX file prepared by the author.